Characterization of electronic conductivity by broadband dielectric spectroscopy of positive electrode materials of Spinel-type Li-ion batteries

Internship report/ Master thesis

by

Mahmoud Aboaouf

Surface, Electro-, Radiation, and Photo-Chemistry (SERP+)

February-July 2024

Supervised by:

Dr. Olivier Dubrunfaut

Dr. Nicolas Emery

Dr. Jean-Claude Badot

Dr. Stéphane Bach

Table of content

Abstract

Despite their high theoretical specific capacity (~147 $mAh.g^{-1}$), their high operating voltage (~4.7 V) and the absence of cobalt in their compositions, positive electrode materials with a $LiMn_{2-x}Ni_xO_4$ (LMNO) spinel structure have not yet been incorporated into commercial batteries. This is partly due to an incomplete understanding of the correlation between their structure and their electrochemical performance. In this study, we investigate the electronic conductivity and its mechanism in a series of LMNOs with varying Ni content (0.50, 0.45, 0.40 and 0.35) synthesized under conditions limiting the presence of structural defects.

The electronic conductivity of pristine materials has been depicted by combining analysis of galvanostatic and Broadband dielectric spectroscopy (BDS) measurements. The galvanostatic measurements provides insight on the overall voltage evolution and on the Mn^{3+} content of the reduced phase while BDS experiments provides the grain conductivity and permittivity, which is intrinsic to the probed composition. A fine analysis of the galvanostatic curves recorded at slow rate suggests the presence of two different types of Mn^{3+} for samples with nickel content lower than 0.5. BDS experiments evidence the conductivity of the grain increase with the number of mobile charge carrier, which is directly correlated to the Mn^{3+} content. Finaly, from permittivity measurements, it is speculated that clusters form a percolation network within the grain in between Ni content of 0.45 and 0.40.

Keywords: Li-ion battery, electronic conductivity, Broadband Dielectric Spectroscopy, spinel, electrochemical performance

---

Résumé :

Malgré une capacité spécifique théorique élevée (~147 $mAh.g^{-1}$), leur tension de fonctionnement élevée (~4,7 V) et l'absence de cobalt dans leurs compositions, les matériaux d'électrode positive de structure spinelle $LiMn_{2-x}Ni_xO_4$ (LMNO) n'ont à ce jour pas été intégrés dans des batteries commerciales. Ceci est en partie dû à une compréhension incomplète de la corrélation entre leur structure et leur performance électrochimique. Dans cette étude, nous étudions la conductivité électronique et son mécanisme dans une série de LMNO de teneur en Ni variable (0,50, 0,45, 0,40 et 0,35) synthétisée dans des conditions limitant la présence de défauts structuraux.

La conductivité électronique des matériaux synthétisés a été décrite en combinant l'analyse des mesures galvanostatiques et celles de spectroscopie diélectrique à large bande (BDS). Les mesures galvanostatiques donnent un aperçu de l'évolution globale de la tension et de la teneur en Mn^{3+} de la phase réduite, tandis que les expériences BDS fournissent la conductivité et la permittivité des grains, qui sont intrinsèques à la composition sondée. Une analyse fine des courbes galvanostatiques enregistrées à vitesse lente suggère la présence de deux types différents de Mn^{3+} pour les échantillons dont la teneur en nickel est inférieure à 0,5. Les expériences BDS montrent que la conductivité du grain augmente avec le nombre de porteurs de charge mobiles, ce qui est directement corrélé à la teneur en Mn^{3+}. Enfin, à partir des mesures de permittivité, il est supposé que les clusters forment un réseau de percolation dans le grain entre les teneurs en Ni de 0,45 et 0,40.

Mots-clés : Batterie Li-ion, conductivité électronique, spectroscopie diélectrique à large bande, spinelle, performance électrochimique

1. Introduction

1.1 Background and objective

To follow the European union's objective of reduction greenhouse gases emissions by 55% by 2030, large efforts are focused on developing batteries for electrical vehicles [1]. It is the actual most mature green technology for mobile applications. One of the good candidates to be commercialized for this technology is the $LiMn_{1.5+x}Ni_{0.5-x}O_4$ (LMNO) spinel materials family. Due to their high theoretical specific capacities (~147 $mAh.g^{-1}$) and their high operation voltage (4.7 V vs Li^+/Li), these materials are attractive for high power applications such electrical vehicles [2]. Moreover, the absence of cobalt, which is a critical raw material, in their composition compared with conventional NMC cathodic materials is a true asset. Despite the mentioned advantages, the LMNO materials are not yet commercialized. It is partly due to a misunderstanding of the structure/electrochemical relationship, which is not yet clearly established. The nickel composition and/or the structural defect density affect the electrochemical response and it is strongly influenced by the synthesis procedure. The richest nickel composition, $LiMn_{1.5}Ni_{0.5}O_4$, exhibits two different electrochemical curves, depending on the temperature of the thermal treatment [3], if it is prepared at 700°C (black curve, Figure.1) or at 900°C (red curve).

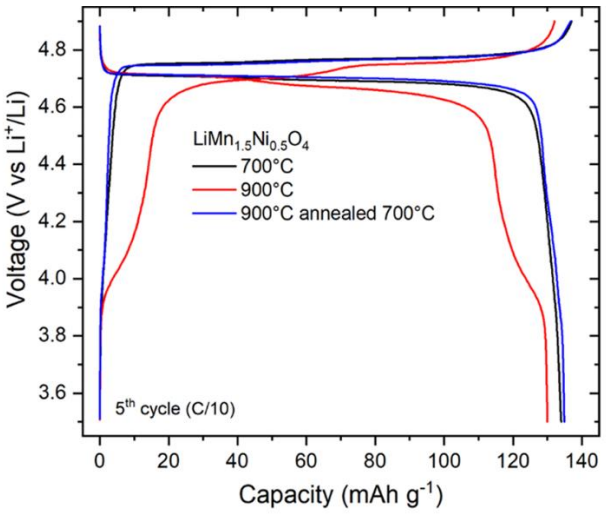

Figure.1: Galvanostatic measurements of $LiMn_{1.5}Ni_{0.5}O_4$ synthesized at different conditions [3].

The electrochemical curve of the $LiMn_{1.5}Ni_{0.5}O_4$ prepared at 700°C exhibits two voltage plateaus around 4.7V corresponding to the oxidation/reduction of the $Ni^{2+/}Ni^{3+}$ and Ni^{3+}/Ni^{4+} redox couples. The electrochemical curve of the $LiMn_{1.5}Ni_{0.5}O_4$ prepared at 900°C displays these two voltage plateaus but with significant voltage difference between them and, around 4.2V, an additional contribution attribute to the oxidation/reduction of a variable amount of Mn^{3+} present in the pristine material. Such a contribution is not expected in a stoichiometric $LiMn_{1.5}Ni_{0.5}O_4$ compound and one can see that the specific capacity is slightly lower than the sample prepared at 700°C. It was attributed to the formation of a spurious phase rich in nickel and electrochemically inactive. The formation equation of this rock-salt impurity explains both the mass loss observed from TGA experiment and the lower specific capacity regards to the sample prepared at 700°C (eq.1).

$$LiMn_{1.5}Ni_{0.5}O_4 \leftrightarrows n\ LiMn_{1.5+x}Ni_{0.5-x}O_4(\text{spinel phase}) + m\ Li_y\ (Ni_{0.67}Mn_{0.33})_{1-y}O\ (\text{FCC phase}) + k\ O_2 \quad (eq.1)$$

An important point to mention is that this secondary phase formation occurs in the same range of temperature as the temperature required to have a grain's growth (above 750 °C). Hence, the synthesized samples prepared at higher temperature may have different amount of rock-salt impurities. A solution to remove this rock-salt impurity is to add an annealing step at 700°C after the initial calcinating step at 900°C. As a result, grain's growth is obtained and the rock-salt phase is eliminated: the resulting electrochemical curve is then similar to the curve obtained after a synthesis at 700°C (blue curve, Figure.1, [3]).

Moreover, the structural ordering is strongly affected by the synthesis conditions. Once the sample has been prepared or annealed at 700°C, $LiMn_{1.5}Ni_{0.5}O_4$ displays a reverse spinel structure within the space group $P4_332$. In such a description, each transition metal ion fills its own site and a long-range ordering between Ni and Mn ions occurs [2]. Once prepared at higher temperature, an apparent spinel phase is obtained, within the space group Fd-3m. In such a description, Ni and Mn ions are randomly distributed in the filled octahedral site. Hence, two neighboring filled octahedrons can accommodate a nickel ion [4]. During the past decade, it has been demonstrated that locally, the "ordered" $P4_332$ structure is conserved, which does not allow two neighboring octahedral sites filled by Ni ions [3,5] and the apparent "disordered" Fd-3m structure is due to a strong density of planar defect called Antiphase Boundary [3,6].

These subtle structural differences led to a little understanding of the LMNO material family, particularly in the correlation between the structure, its conductivity mechanism, and the electrochemical performance. Therefore, since both the composition and the defect density are susceptible to affect the electrochemical properties, the aim of this project is to study first the effect of only the nickel composition on the electrochemical properties. To this purpose, and to reduce the defect density, a two steps synthesis protocol has been used with a systematic annealing time. The obtained samples with different nickel compositions were analyzed by X-ray diffraction (XRD), Galvanostatic measurements, Broadband dielectric spectroscopy (BDS), with supports of preliminary DFT calculations (performed by the MSME laboratory, partner of the project).

Broadband Dielectric Spectroscopy is not a common tool for material characterization but is extremely powerful since it allows to discriminate the different contribution to the conductivity/permittivity spectrum.

1.2 Broadband dielectric spectroscopy

Broadband dielectric spectroscopy is a perturbation technique that measures the complex relative permittivity ($\varepsilon^*(\omega) = \varepsilon'(\omega) - i\,\varepsilon''(\omega)$), where $\varepsilon'(\omega)$ and $\varepsilon''(\omega)$ are the real and imaginary parts of complex permittivity, respectively. The perturbation is done by probing the material under investigation with a transverse electromagnetic wave in a frequency range of 10^{-6} - 10^{12} Hz [7] (generally). Materials could be probed by low amplitude Electromagnetic field. In the case of this study, LMNO is a semiconductor which has no magnetic properties, so, its response is due to stimulation by the Electric field vector ($\vec{E}$ / V.m^{-1}) of the electromagnetic wave. As a response to this perturbation, the material gets polarized ($\vec{P}$) due to dipoles motion of charge carriers (electrons and/or ions). The response will be linear by applying low amplitude electromagnetic wave as shown in eq.2 [8]. ε_0 is vacuum permittivity = 8.84×10^{-12}/F.m^{-1}, ω is radial frequency/ Rad.s^{-1}.

$$\vec{P} = \varepsilon_0(\varepsilon^*(\omega) - 1)\ \vec{E}\ (eq.2)$$

In this study, the range of frequency used is between 20 Hz–10 GHz. Therefore, relaxation processes (due to polarization) could be resolved at different scales (from macroscopic to interatomic scale), as the higher the frequency, the smaller the size that could response as shown in Figure.2.

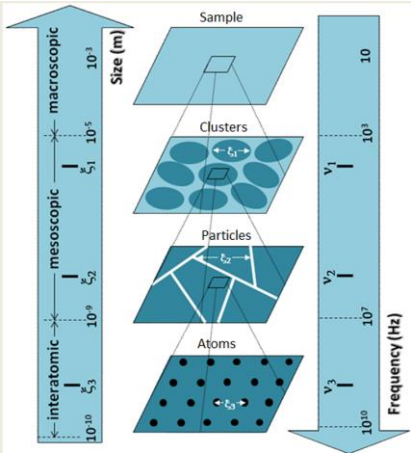

Figure.2: polarization at different scales with variation of frequency [9].

The polarization could be generalized as in eq.3, where m is the number of relaxation processes.

$$\vec{P}_{Total} = \vec{P}_1 + \vec{P}_2 + \cdots . + \vec{P}_m \ (eq.3)$$

By solving the first order differential equation (eq.4a), one can obtain the complex permittivity as a function of frequency (Debye model) in eq.4b [10], where τ_d is the characteristic relaxation time for a relaxation process, ε_∞ is the real part permittivity at the high frequency end of the relaxation process, and $\Delta\varepsilon$ is the dielectric strength of the polarization process.

$$\frac{d\vec{P}(t)}{dt} = -\frac{1}{\tau_d}\vec{P}(t) \text{ (eq.4a)} \qquad \varepsilon^*(\omega) = \varepsilon_\infty + \frac{\Delta\varepsilon}{1+(i\omega\tau_d)} \text{ (eq.4b)}$$

However, it is rare to observe a Debye relaxation process, as it assumes a distinct relaxation time (only valid in ideal systems). So, eq.4b could be extended empirically into eq.5 (Havriliak–Negami function) to consider a distribution of the relaxation times. Where α and β are fitting parameters. The equation reduces to Debye model when α=1 and β = 1, Cole-Cole model (assumes symmetric broad distribution of τ) when $\alpha \neq 1$ and β = 1, and Cole-Davidson model (assumes asymmetric broad distribution τ) when $\alpha = 1$ and $\beta \neq 1$ [11].

$$\varepsilon^*(\omega) = \varepsilon_\infty + \frac{\Delta\varepsilon}{(1+(i\omega\tau)^{1-\alpha})^\beta} \ (eq.5)$$

Taking eq.5 into consideration a complex permittivity spectra of multiple polarization processes (eq. 3) could be modeled as eq.6.

$$\varepsilon^*(\omega) = \varepsilon_\infty + [\sum_m \frac{\Delta\varepsilon_m}{(1+(i\omega\tau_m)^{1-\alpha_m})^{\beta_m}}] \ (eq.6)$$

Finally, eq.6 could be further extended into eq.7 to consider a low frequency polarization process that cannot be modeled (due to disorder in long-term conducting network) by adding the term $A(i\omega)^{s-1}$, where A and s are empirical fitting parameters, and the value of $\varepsilon^*(\omega)$ at $\omega \to 0$, which is $\frac{\sigma_{dc}}{i\omega\varepsilon_0}$, where σ_{dc} is the DC conductivity (S.m^{-1}) of the material [12]. A simplified Decomposition of Nyquist complex permittivity plot of a semiconductor using eq.7 could be sketched as shown in Figure.3.

$$\varepsilon^*(\omega) = \varepsilon_\infty + [\sum_m \frac{\Delta\varepsilon_m}{(1+(i\omega\tau_m)^{1-\alpha_m})^{\beta_m}}] + A(i\omega)^{s-1} + \frac{\sigma_{dc}}{i\omega\varepsilon_0} \quad (eq.7)$$

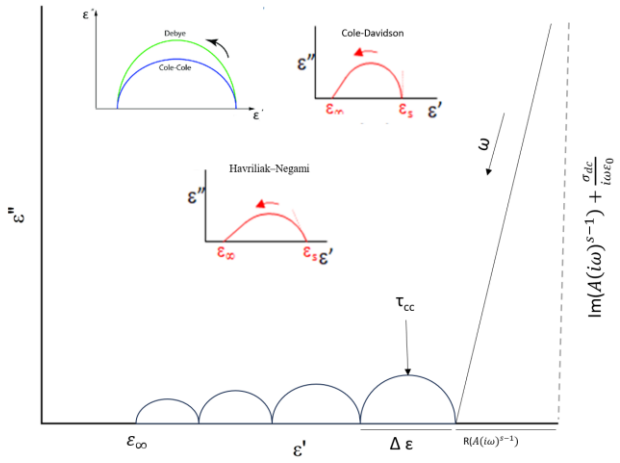

Figure. 3: Simplified decomposition of Nyquist complex permittivity plot for a semiconductor assuming 4 Cole-Cole relaxation processes, and sketches of the behavior of different models [13]. R and Im of $A(i\omega)^{s-1}$ are the real and imaginary part of the term, respectively.

The complex conductivity ($\sigma^*(\omega) = \sigma'(\omega) + i\sigma''(\omega), S.m^{-1}$) spectrum could be modeled by solving the time-dependent electric field equation (eq.8a) into the relation between the current density (J / A.m^{-2}) and the applied electric field (eq.8b). The first term in (eq.8b) represents the induced current density from the free charges (i.e. ions and/or electrons), and the second term is the induced current density due to particle movement as a response to applied sinusoidal electric field [12].

$$\vec{E}(t) = E\, e^{i\omega t} \quad (eq.8a)$$

$$\vec{J}(t) = \sigma_{DC}\vec{E}(t) + \frac{dD}{dt}, D \text{ / } C.m^{-2} \text{is the displacement field } \left(D = \varepsilon_0\varepsilon^*\vec{E}(t)\right) \quad (eq.8b)$$

From the solution (eq.9), the relation between the real part of conductivity with the imaginary part of permittivity (eq.10a), and the relation between the imaginary part of conductivity and the real part of permittivity (eq.10b) could be derived. Thus, similar to the idea of complex permittivity spectrum, the conductivity spectrum could be decomposed to estimate the conductivity contribution for each relaxation process.

$$\vec{J}(t) = (\sigma_{DC} + i\omega\varepsilon_0\varepsilon^*)\,\vec{E}(t) \quad (eq.9)$$

$$\sigma^*(\omega) = \sigma_{DC} + i\omega\varepsilon_0\varepsilon^*$$

$$\sigma' = \sigma_{DC} + \omega\varepsilon_0\varepsilon^{"} \ (eq.10a)$$

$$\sigma^{"} = \omega\varepsilon_0\varepsilon' (eq.10b)$$

2. Methods

2.1 Synthesis

4 gm of $LiMn_{(2-x)}Ni_xO_4$ Samples of 0.5, 0.45, 0.40, 0.35, and 0.3 Ni stoichiometry were synthesized by co-precipitation of metals acetates (> 99% Sigma-Aldrich) mixed with oxalic acid of 1:1 molar ratio to metals ions. The precursors were precisely weighted, dissolved in distilled water, followed by stirring until reaching clear green solutions. The solutions were dried at 110 °C to obtain the precipitants which were first burned at 450 °C for 6 h to remove the organic species. The as-obtained black powders were pressed into 13 mm pellets using hydraulic piston, followed by a thermal treatment at 900 °C for 12 hours. Pellets were then thoroughly ground and die-pressed again to ensure a good chemical homogeneity. These samples were heated at 900°C for 12 h and then annealing at 700°C for 4 days. The experimental weights of the starting materials used in these syntheses, as well as molecular formulas and IDs of the products (used to identify specific samples), are shown in Table.1.

Table 1: mass of chemical reagents to prepare variable nickel content $LiMn_{2-x}Ni_xO_4$ spinel compounds.

Molecular formula	ID	$CH_3COOLi.2H_2O$ (gm)	$(CH3COO)_2Mn.4H_2O$ (gm)	$(CH3COO)_2Ni.4H_2O$ (gm)	$(COOH)_2.2H_2O$ (gm)
$LiMn_{1.50}Ni_{0.50}O_4$	LMNO-50	2.233(5)	8.049(4)	2.724(4)	8.281(2)
$LiMn_{1.55}Ni_{0.45}O_4$	LMNO-45	2.236(1)	8.326(4)	2.454(3)	8.289(0)
$LiMn_{1.60}Ni_{0.40}O_4$	LMNO-40	2.238(5)	8.603(2)	2.183(6)	8.297(0)
$LiMn_{1.65}Ni_{0.35}O_4$	LMNO-35	2.240(9)	8.881(1)	1.913(2)	8.306(3)
$LiMn_{1.70}Ni_{0.30}O_4$	LMNO-30	2.242(8)	9.160(6)	1.641(8)	8.314(9)

2.2 XRD and SEM/EDS

Panalytical XPert Pro diffractometer equipped with Co X-ray tube (λKα=1.789Å) and a Pixcel 1D linear detector was used for powder-Xray data acquisition of LMNO samples. The evolution of the cell parameter of the samples was obtained by refining the cell parameter using GSAS ExpGUI software within the Rietveld method [14]. Information about the morphology of the grains was obtained with a Zeiss Merlin scanning electron microscope equipped with Energy-Dispersive X-ray detector for atomic composition analysis.

2.3 Galvanostatic measurements

Pastes of these positive electrode materials were prepared by mixing thoroughly weight fractions of 80% of the active materials (LMNO-50, LMNO-45, LMNO-40, and LMNO-35), 10% of polytetrafluoroethylene (PTFE) binder, and 10% of acetylene black with acetone until evaporation.

5-8 mg of each paste was pressed on a stainless-steel grid (act as a current collector) using a hydraulic press. The cathodes of the mentioned materials, a 14 mm diameter Li foil (functioning as both the negative and reference electrode), and three Whatman separators that were soaked with 1 M $LiPF_6$ electrolyte solution were used in two-electrode CR2032 coin cells assembled in a glovebox filled with argon atmosphere. The galvanostatic measurements were collected using a VMP3 Biologic potentiostat at 20 °C. Galvanostatic measurements started after an hour of open circuit relaxation to reach the electrochemical equilibrium, followed by 3 cycles of C/5 charge/discharge rate (1 Li^+ exchange in 5 hours) then 10 cycles of C/30 charge/discharge rate. C/5 cycles are used to form the solid electrolyte interphase since both lithium and the spinel are outside of the electrochemical window of the electrolyte. Then, slow rate cycles are performed to be as close as possible to the thermodynamic equilibrium.

2.4 EX-situ BDS

2.4.1- Sample preparation

Two methodologies were adapted to prepare 3mm cylindrical pellets of LMNO-50, LMNO-45, LMNO-40, and LMNO-35 with thickness in-between 0.50-0.95 mm. The first one is by grinding the powder of the sample with 3%wt of PTFE, then a relevant weight of the mixture was pressed under a pressure of 0.7 GPa using hydraulic press. For the second methodology, only the powder was pressed under a pressure of 0.7 GPa, followed by sintering at a temperature of 900 °C for 12 hrs followed by an annealing step at 700 °C for four days. The sintering process was done to ensure that the pellets have good mechanical stability for sample handling, and introduction to BDS apparatus. Both types of pellets were coated with silver paste on both sides (to have a homogenous electrical contact in the APC7 cell) and heated on a hotplate with a temperature around 80 °C to eliminate the solvent residue of the paste.

2.4.2- BDS apparatus

Before a sample measurement, a relevant calibration to eliminate systematic error was carried out using Agilent calibration kit that contain a load of 50 Ω, an open circuit, and a short circuit. A sample pellet and a disk-shaped sample holder were then placed on a short-circuit that is connected with a coaxial wave guide as shown in Figure.4. Transverse electromagnetic waves with frequency range of 20 Hz 10 GHz were generated by an excitation port at the input of the coaxial guide using two analyzers. The first is an impedance analyzer (Keysight 4990, low-frequency analyzer) that generates electromagnetic waves with a frequency range of 20 Hz – 120 MHz, while the other is a network analyzer (Agilent E8364B, High-frequency analyzer) that produces frequency range of 50 MHz –18 GHz. The complex admittance (Y^* in S) is related to the reflection coefficient (Γ) of the reflected electromagnetic wave as demonstrated in eq. 11, where Y_0 is equal to 0.02 S (the admittance of the coaxial waveguide [15]).

$$Y^* = Y_0 \frac{1-\Gamma}{1+\Gamma} \quad \text{(eq.11)}$$

The overlap between the two analyzers was taken in a frequency range between 80 MHz – 120 MHz to assess the agreement of the measurements. In this study, however, a poor agreement between the two analyzers was found as the samples' conductivities were below the sensitivity of the high-frequency analyzer. Fortunately, most of the information needed could be interpreted in the low-frequency analyzer range as will be discussed.

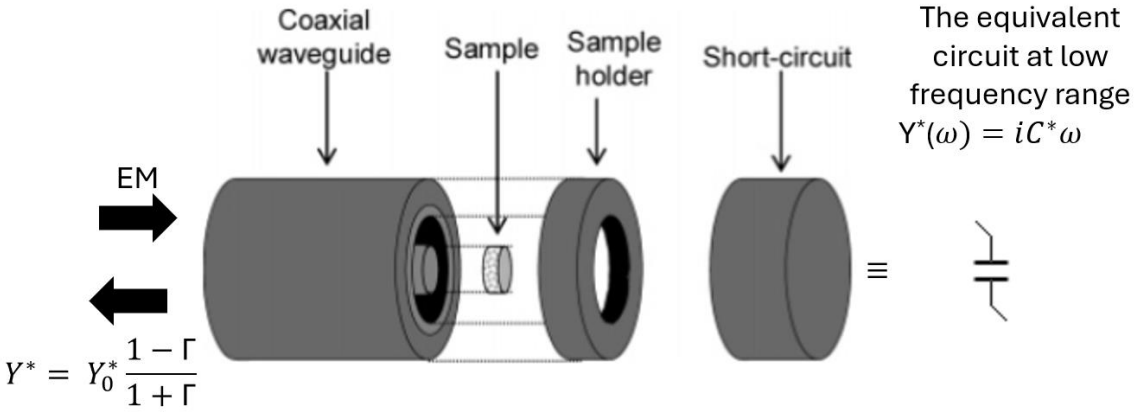

Figure 4: BDS cell [16]: The coaxial waveguide connection with the cell that contains the sample, and the equivalent circuit of the discontinuity of the coaxial waveguide and the short circuit at low frequency. For high frequency it is more complex [17].

2.4.3- BDS data acquisition and analysis

After calibration, LMNO-50, LMNO-45, LMNO-40, and LMNO-35 were measured at Room temperature, and in-between 200 K – 290 K using dry nitrogen flux (except LMNO-35). The complex permittivity and conductivity spectra were calculated from the complex admittance $Y^*(\omega)$ (that is measured by the apparatus) using homemade software. The spectra of the sintered and powder-binder pellets were compared to ensure that there is no change in the electronic and/or the structure of the composition under investigation (as will be discussed in the results section). After confirming that there is no change only the sintered pellets data were analyzed. The first step is analyzing the resistivity Nyquist plot ($\rho''(\omega)$ vs $\rho'(\omega)$) to estimate the conductivity mechanism of the samples and the resistivity of each contribution (sample interface, grain boundary, grain, …) by determining the equivalent circuit (similar to impedance Nyquist, it could be used to fit complex resistivity [12]) in the low frequency range. This was done by building a custom Python script based on "impedance" library [18] (a pre-made library that includes the mathematical description and fitting of equivalent circuits). The idea of the script is to make trial, measure error, and improve cycles (iteration) by providing a reasonable bound of a desired equivalent circuit's parameters. After trying different error functions to be used in the iteration, the optimum error function found was Normalized root mean square (NRMS) as it gave the best fitting (according to the correlation factor, R^2). The number of iterations was determined based on the quality of the data and the complexity of the equivalent circuit that is used for fitting. In all cases, the number of iterations used ensures reaching a stable solution, and the quality of the fit was assessed by the average correlation factor (R^2 of the $\rho'(\omega)$ and $\rho''(\omega)$). After analyzing the resistivity plots and evaluating the resistivity contribution at each scale, the first resistivity contribution (that is at low frequency range) is removed from the complex permittivity spectra (if possible) using the homemade software to ensure approaching the scale of interest (which is the sub-grain, and the interatomic scale as will be discussed) with a high precision. For example, removing the interfacial

contribution to resistivity removes the sample polarization contribution in permittivity. The interpretation of the permittivity at such scales would give information about the charge dynamics that is responsible to the conductivity.

3. Results and discussion

3.1 X-ray diffraction

The XRD patterns of the synthesized LMNO samples are shown in Figure. 5a. The sharpness of the peaks shows the high crystallinity of the materials. The cell parameter linearly increases with decreasing the Ni content as shown in Figure. 5b, which is consistent with previous studies [3,19].

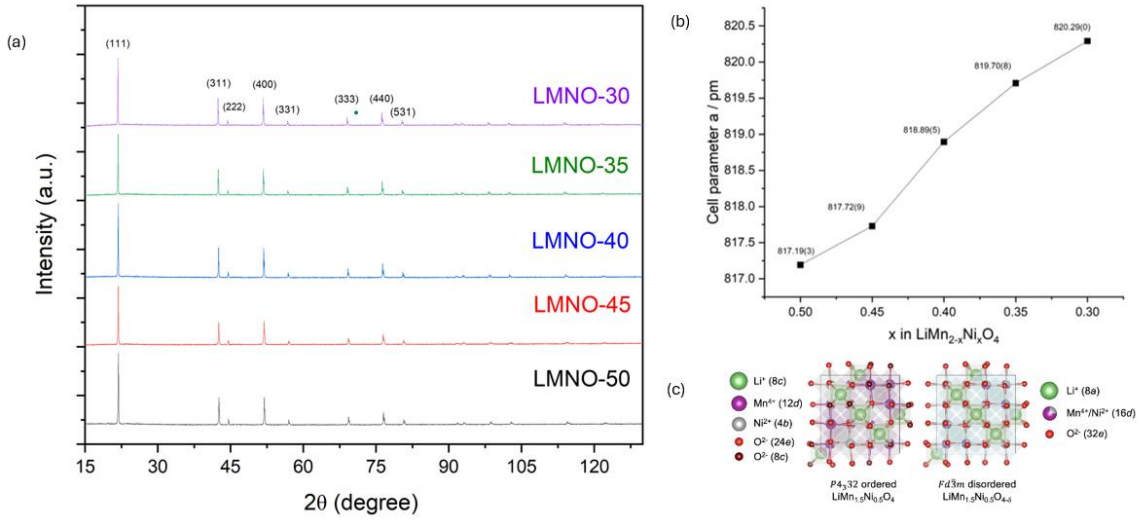

Figure 5: (a): XRD patterns of the LMNO samples. (b): the evolution of the cell parameter with the theoretical Ni content. (c): The ordered and the disordered structure of LMNO-50 [20].

It is attributed to the different sizes of Ni^{2+} (69 pm), Mn^{3+} (64.5 pm) and Mn^{4+} ions (54 pm) [21]. Hence, the substitution of a Ni^{2+} ion by a Mn^{3+} ion induces the formation of second Mn^{3+} ions, which induces a dilation of the average size of the transition metal cations. The peaks indexing shows an apparent Fd-3m space group (observed for the "disordered" structure where the transition metal cations are randomly distributed in the octahedral sites of the spinel structure). However, according to the literature [3], with our synthesis conditions, the space group of the materials should be $P4_332$ (observed for ordered transition metal cations distribution). The cell units of ordered and disorder LMNO-50 is shown in Figure. 5c.

3.2 Scanning electron microscopy

SEM images of the LMNO series shown in Figure.6 show a high degree of crystallinity of the materials, as the crystals show octahedral shape as expected. Well faceted samples with micrometric grains are obtained thanks to the 900°C step during the synthesis protocol. According to [22]. Temperature higher than 750°C are needed to obtain a grain's grow while the annealing step leads to an ordered distribution of Ni and Mn ions within the octahedral site of the spinel structure.

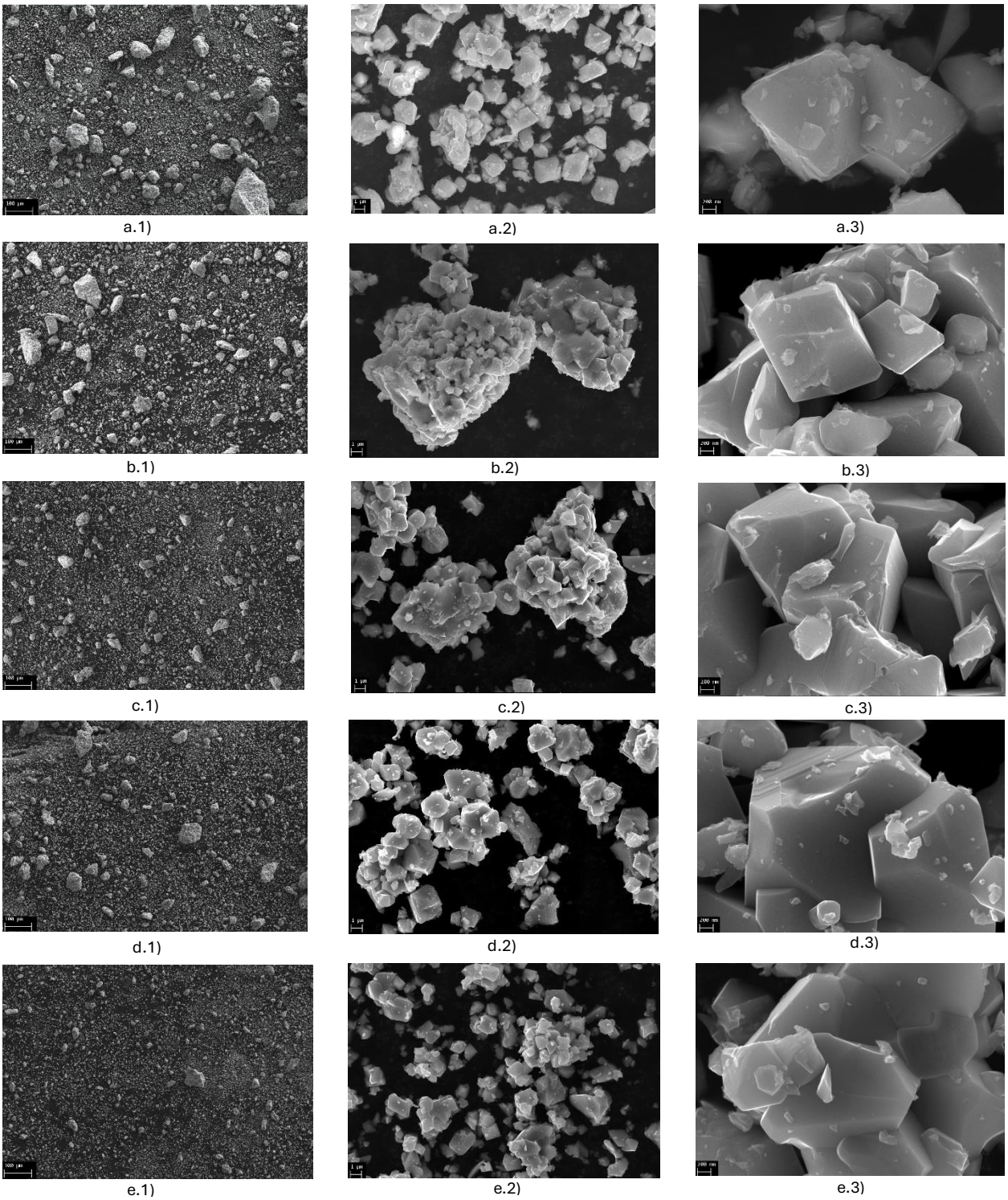

Figure 6: SEM images of (a) LMNO-50, (b) LMNO-45, (c) LMNO-40, (d) LMNO-35, and (e) LMNO-30 at magnification of (1) 100X, (2) 4000X, and (3) 25000X.

3.3 EDS

Energy dispersive spectra were collected on 4 different points to check the sample homogeneities and to evaluate the Ni/Mn ratio. Table 2 gathers the expected Ni/Mn ratio and those extracted from the EDS analyses. It can be seen that the experimental ratio is consistent with the expected one.

Table 2: Expected Ni/Mn ratio compared to the experimental ratio extracted from EDS measurements (4 points average).

Sample	Expected Mn/Ni	Experimental Mn/Ni ratio
LMNO-50	3.00	2.99 ± 0.03
LMNO-45	3.44	3.50 ± 0.06
LMNO-40	4.00	4.02 ± 0.05
LMNO-35	4.71	4.72 ± 0.05
LMNO-30	5.67	5.66 ± 0.09

3.4 Galvanostatic measurements

The galvanostatic curves recorded in oxidation at C/30 rate for LMNO series are gathered in Figure. 7. The specific capacities extracted from these curves for LMNO-50, LMNO-45, LMNO-40, and LMNO-35 are 139, 135, 127, and 137 mAh.g^{-1}, respectively. These experimental values are in line with the theoretical capacity of the LMNO series is around 147 mAh.g^{-1}.

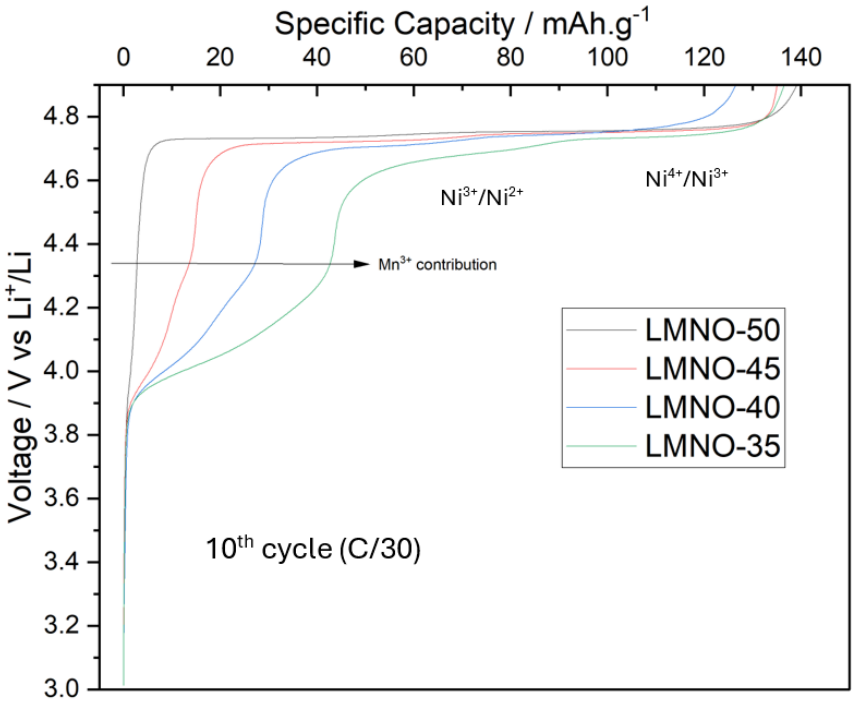

Figure 7: galvanostatic measurements of charging (oxidation) at the 10th C/30 cycle for different nickel compositions

As expected, a contribution between 4 and 4.2 V increases at the expense to the 4.7 V contributions with decreasing Ni content. Since the less the Ni^{2+} content, the more the Mn^{3+} content to maintain the charge neutrality, the 4-4.2 V contribution is attributed to the oxidation of Mn^{3+} to Mn^{4+}. At

around 4.6 V, two potential plateaus appear. They correspond to the Ni^{3+}/Ni^{2+} and Ni^{4+}/Ni^{3+} redox couples, respectively. The charge/discharge equation of each redox couple is represented as follows:

Mn^{4+} / Mn^{3+} : $$LiMn_{2-x}Ni_xO_4 \leftrightarrows Li_{2x}Mn_{2-x}Ni_xO_4 + (1-2x)Li^+ + (1-2x)e^-$$

Ni^{3+} / Ni^{2+} : $$Li_{2x}Mn_{2-x}Ni_xO_4 \leftrightarrows Li_xMn_{2-x}Ni_xO_4 + xLi^+ + xe^-$$

Ni^{4+} / Ni^{3+} : $$Li_xMn_{2-x}Ni_xO_4 \leftrightarrows Mn_{2-x}Ni_xO_4 + xLi^+ + xe^-$$

To determine the actual stoichiometry of the prepared LMNO series, the derivative of the capacity with respect to the voltage (dQ/dV) was calculated. The derivative curve helps to estimate the voltage of the Mn^{3+} depletion, thus, estimating the normalized contribution of the Mn^{3+} and all the Ni content to the capacity by finding the intersection of the Mn^{3+} depletion voltage and the stoichiometry of Li during charging as adapted from a previous study [23].

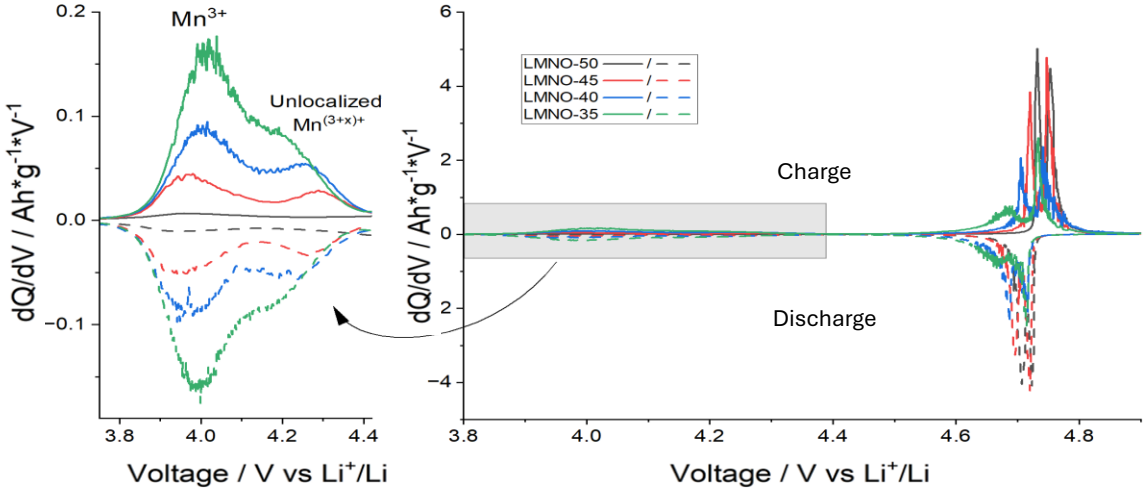

Figure 8: The capacity derivative with respect to voltage (dQ/dV) vs Voltage against Li electrode during charge (top) and discharge (bottom). Right, the whole voltage range. Left, considering only Mn^{4+}/Mn^{3+}.

Figure. 8, shows the derivative curve of the Mn^{4+}/Mn^{3+} redox reaction. In the case of LMNO-45, LMNO-40, and LMNO-35, there are two redox populations in between 3.8 and 4.4 V attributed to the Mn^{3+} oxidation. According to preliminary DFT calculation performed by collaborators, the first contribution in between 3.9 to 4.1 V corresponds to the redox of Mn^{4+} / Mn^{3+} couple, while in between 4.1 to 4.4 corresponds to the oxidation of 6 $Mn^{3.83+}$ ions per Ni^{2+} ion substituted. Indeed, the substitution of a Ni^{2+} by a Mn^{3+} is unbalanced and a second electron as to be distributed. To not drastically disturbs the surrounding ions, it seems that it is more favorable to delocalize this second electron on Mn^{4+} ions which are around the substituted nickel site (Figure. 9). The voltage at which the intermediate oxidation state of Mn gets oxidized is higher simply because for a given redox active species in a structure, lower is the oxidation states lower is the oxidation voltage.

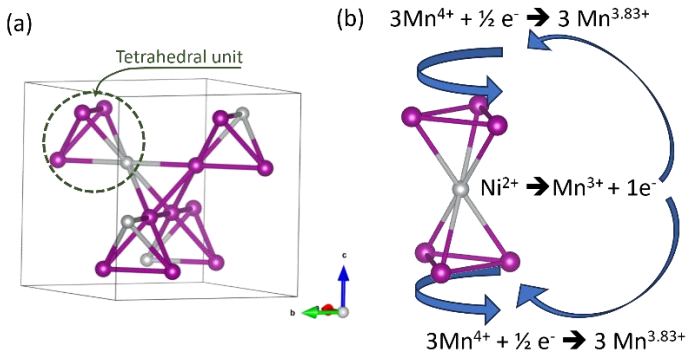

Figure 9: (a) the tetrahedral unit of the cations where Ni^{2+} is white and purple is $Mn^{3.83+}$. (b) demonstration of the effect of Ni^{2+} substitution with Mn^{3+} effect on the electronic structure [24].

The depletion voltage of the mentioned materials is estimated to be 4.38 V. In the case of LMNO-50 only the population of Mn^{4+}/Mn^{3+} was observed which deplete at 4.18 V. The intersection between Li stoichiometry and the depletion voltage corresponds to the point at which Mn^{3+} is fully oxidized in Mn^{4+} (the value of Ni normalized contribution to capacity) is shown in Figure. 10.

Ni, the total Mn, and Mn^{3+} stoichiometric coefficients (v) could be calculated from equations (12), (13), and (14), respectively. Calculated stoichiometries are summarized in Table.3.

$$v(Ni) = \frac{Ni\ normalized\ capacity\ contribution}{2} \quad \text{eq (12)}$$

$$v(Mn) = 2 - v(Ni) \quad \text{eq (13)}$$

$$v(Mn^{3+}) = 1 - Ni\ normalized\ capacity\ contribution \quad \text{eq (14)}$$

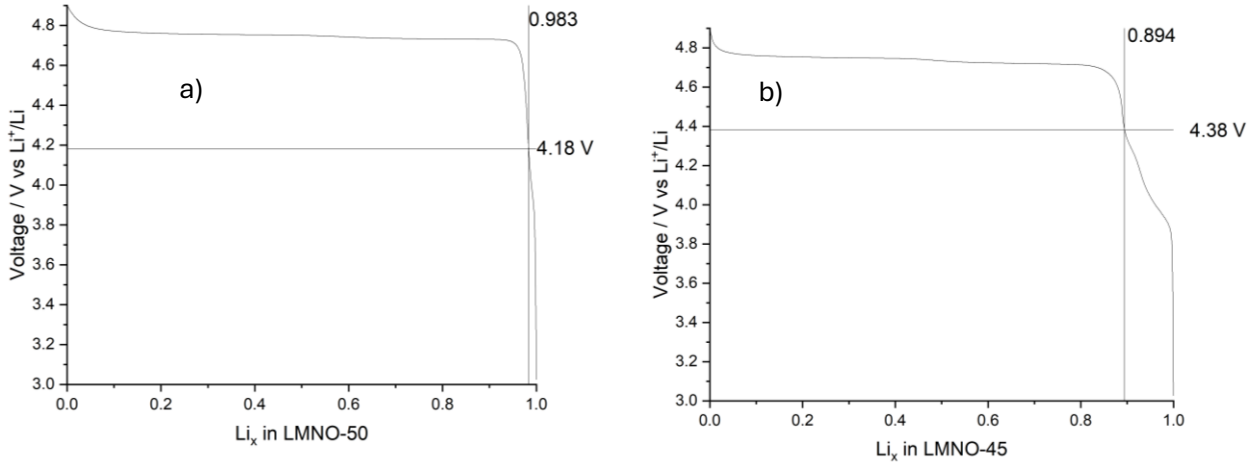

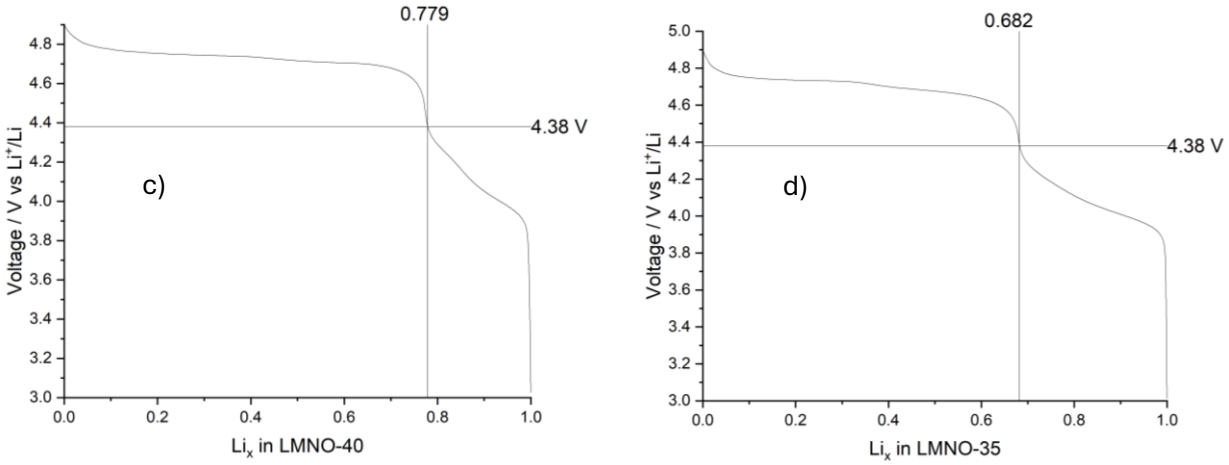

Figure 10: Voltage vs Li stoichiometry for (a) LMNO-50, (b) LMNO-45, (c) LMNO-40, and (d) LMNO-35

Table. 3: The actual stoichiometry of LMNO samples evaluated from the galvanostatic measurements.

Sample	**Actual stoichiometry**
LMNO-50	$LiMn^{4+}_{1.49(2)}Mn^{3+}_{0.01(7)}Ni^{2+}_{0.49(2)}O_4$
LMNO-45	$LiMn^{4+}_{1.44(7)}Mn^{3+}_{0.10(6)}Ni^{2+}_{0.44(7)}O_4$
LMNO-40	$LiMn^{4+}_{1.39(0)}Mn^{3+}_{0.22(1)}Ni^{2+}_{0.39(0)}O_4$
LMNO-35	$LiMn^{4+}_{1.34(1)}Mn^{3+}_{0.31(8)}Ni^{2+}_{0.34(1)}O_4$

Information related to the voltage difference between the Ni^{3+}/Ni^{2+} and Ni^{4+}/Ni^{3+} plateaus is obtained from the derivative curves. Figure. 11a-d, indicate represent the derivative of the galvanostatic curves recorded in oxidation (black curves) and reduction (red curves) for all the compositions. The voltage difference between the Ni^{2+}/Ni^{3+} and Ni^{3+}/Ni^{4+} redox processes can be determined by making the determining the voltage difference of the two observed peaks. The lower point between the two peaks corresponds to the inflection point observed between the two plateaus of the galvanostatic curves. Figure. 11e, gathers the average voltage of both Ni redox couples recorded in oxidation (charge) and reduction (discharge) as a function of the Ni content determined from the electrochemical curves. The voltage difference between these two contributions is also reported.

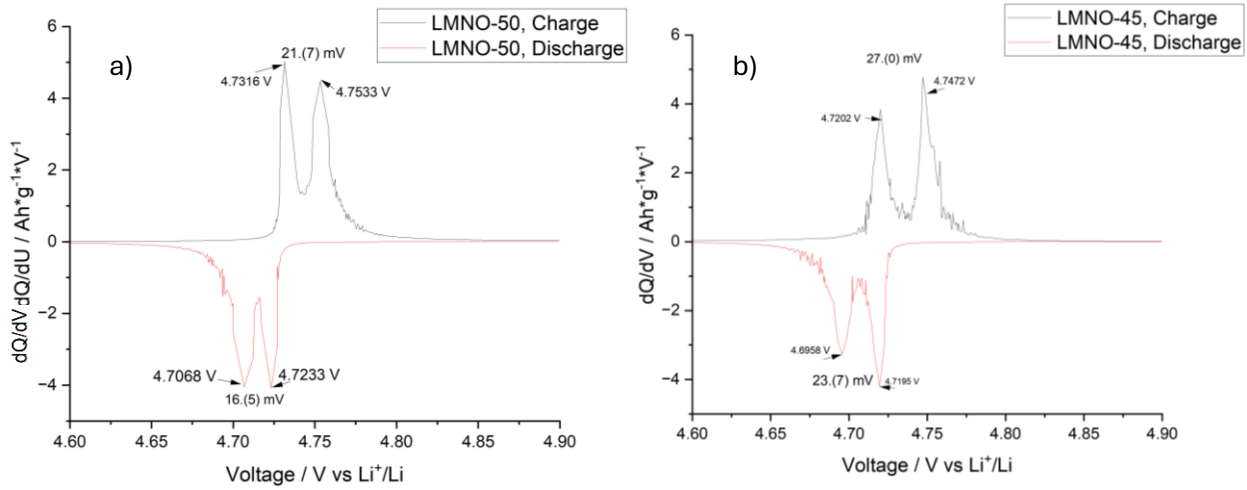

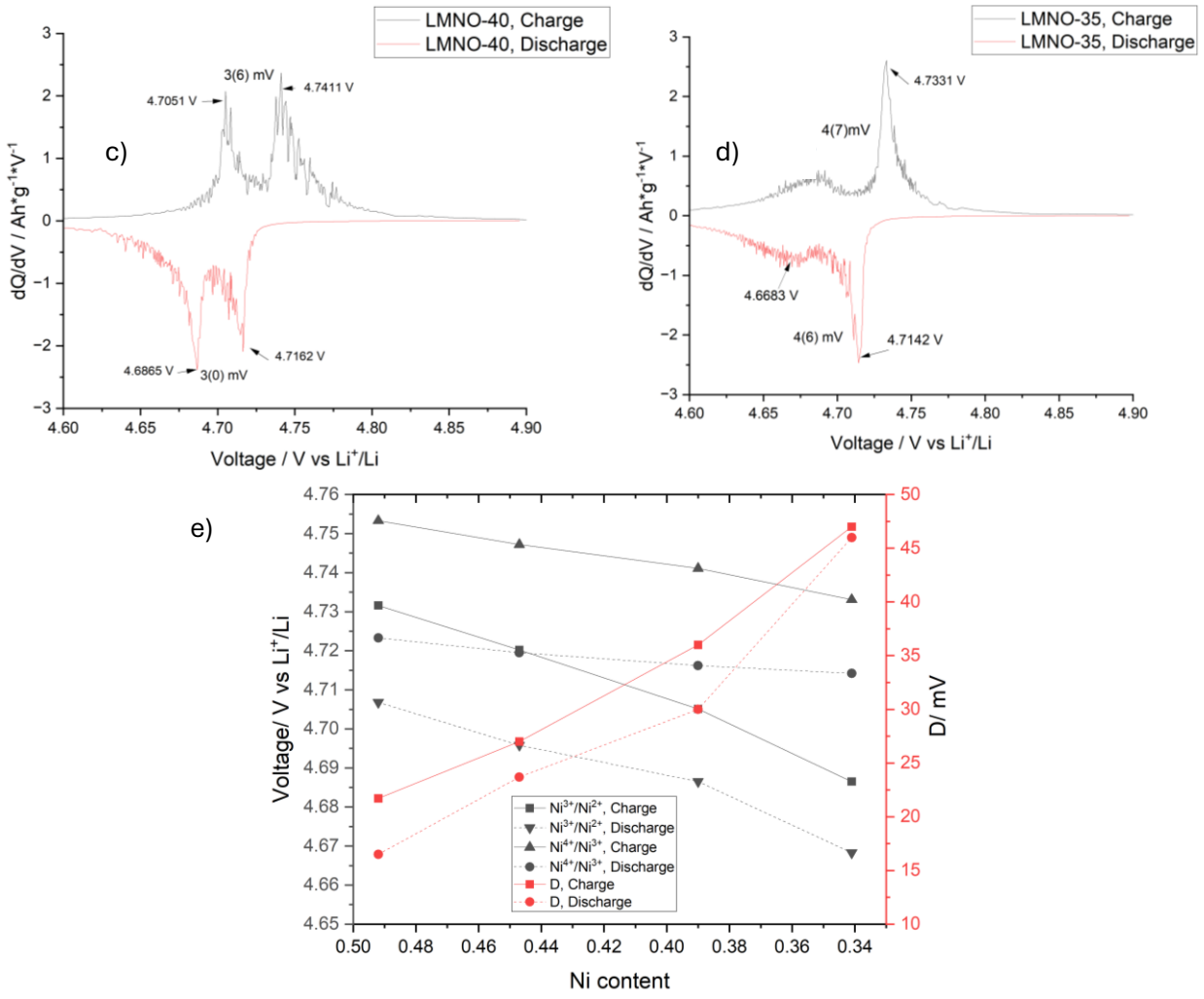

Figure 11: The Ni^{3+}/Ni^{2+} and Ni^{4+}/Ni^{3+} voltage value (in V) and the difference between the two plateaus (in mV) for LMNO-50 (a), LMNO-45 (b), LMNO-40 (c), and LMNO-35 (d). (e) demonstrates the evolution of the plateaus voltage and their difference (D) with decreasing the Ni content

As shown in Figure. 11a, the voltage difference between two Ni redox couples is around 16.5 mV during discharge and 21.7 mV during charge. These values fall into the expected range of an ordered LMNO-50 sample [25]. For disordered LMNO-50 structures, the difference is usually around 50 mV due to the disorder of Ni content and the presence of Mn^{3+} as previously discussed. Figure. 11b-d, indicates an increase separation of these two processes with decreasing nickel content. In addition, the Ni^{2+}/Ni^{3+} contribution becomes broader and broader with decreasing nickel content. It is probably attributed to the occurrence of local disorder since Ni^{2+} has a larger ionic radius than Mn^{4+} ions (69 pm and 54 pm respectively [21]). Conversely, the Ni^{3+}/Ni^{4+} contribution is less affected since Ni^{3+} and Ni^{4+} have similar ionic radii (56 and 48 pm respectively). Figure. 11e exhibits a clear variation of the Ni^{2+}/Ni^{3+} couple while the Ni^{3+}/Ni^{4+} is less affected by the nickel content. Moreover, linear trends are observed for both voltage plateaus with the nickel content, which is a possible indication of this size effect and/or an effect of the

lithium distribution within the structure (the oxidation of Mn^{3+} to Mn^{4+} induced a less symmetric distribution of the lithium ions within the cell than for pure $LiMn_{1.5}Ni_{0.5}O_4$).

3.4 Ex-situ BDS

Measurements were first performed on pellets composed of powder with a small amount of binder (3wt% PTFE). For each sample, real parts permittivity (ε') and conductivity (σ') exhibit several relaxations in the frequency range 20 Hz – 10 GHz (Figure. 12). For all materials, σ' increases and ε' decreases when frequency increases due to lowering the scale of sample's response from millimeteric to sub-nanometric scale, thus, information about the grain and sub-grain properties could be obtained. Since the addition of PTFE induces additional interfaces and therefore, relaxation in the permittivity and conductivity spectra, sintered pellets were produced and measured. Hence, it allows to reduce the number of interfaces and increases the overall conductivity at low frequency without significant modification of the spectra in the high frequency range (Figure 12). Whatever the composition, the sintered pellets exhibit a conductivity at low frequency more than one order of magnitude higher than the pellets made of pressed powder with PTFE. In addition, the real conductivity of both powder and sintered materials aligns at a high frequency which indicates that the sintering process has no effect on the grain properties. The discussion will be therefore focused on data recorded on sintered pellets, since the intrinsic properties of these spinels (i.e. grain conductivity, and interatomic electronic motion) are object of this work. Unfortunately, even though conductivities of the global samples increased with the sintered pellets, they are still below the high-frequency analyzer limits and the measurements are still not precise. It is evident form the overlap between the two analyzers and the noise of the data.

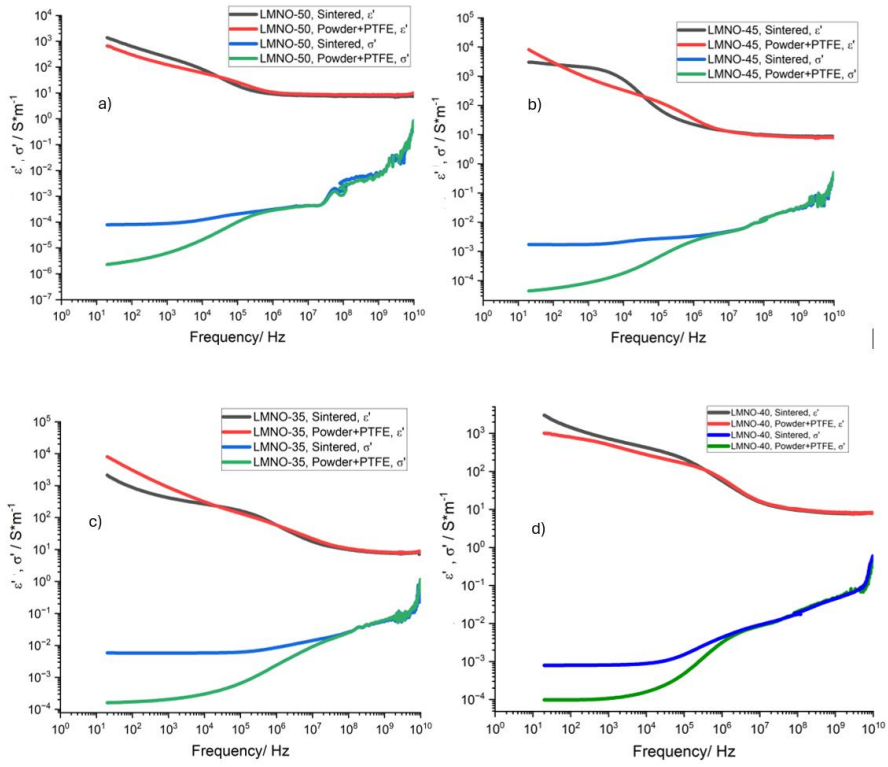

Figure 12: comparison of the real part of permittivity and the real part of conductivity between the sintered and the powder-binder materials. (a) LMNO-50, (b) LMNO-45, (c) LMNO-40, and (d) LMNO-35.

From complex resistivity (derived from complex conductivity), information about the nature of the material's conductivity (i.e. electronic, ionic, or mixed conductivity) can be collected. As shown in Figure. 13a, the Nyquist plots of resistivity could be fitted by a typical equivalent circuit of a series of parallel resistivity and constant phase element components. Each parallel part corresponds to a certain scale depending on the frequency. This type of equivalent circuit corresponds to electronic conductivity [26]. Then, no lithium ionic motion was evidenced from our measurements. It can be simply explained by the lack of available sites for lithium hopping in the pristine material. Indeed, lithium diffusion within these phases needs lithium vacancies, otherwise, electrostatic repulsion between neighboring lithium ions will occurs and the Li^+ ions will remain in their tetrahedral sites. In other words, the phase must be slightly oxidized to initiate lithium motion.

A comparison of sintered materials' conductivity is presented in Figure. 13b. The order of DC conductivity is LMNO-35 > LMNO-45 > LMNO-40 > LMNO-50. It was expected that LMNO-40 sample would have higher DC conductivity than that of LMNO-45. It is probably due to poor interfacial contact and possibly to a higher porosity of LMNO-40 pellet. It is therefore confirmed by the decomposition of the Nyquist plots, where the two lowest frequency contributions to the resistivity, attributed to the high interface and the grain boundary, are significantly higher for the LMNO-45 than for LMNO-40. The highest frequency contribution (green dot curves on Figure. 12c) is attributed to the grain conductivity of the material, i.e. the intrinsic conductivity of the phase. The evolution of this conductivity as a function of the Ni content determined from galvanostatic measurements and therefore, to the Mn^{3+} content, is given in Figure. 13c. The grain conductivity increases linearly with Mn^{3+} content. It is explained by the increasing amount of Mn^{3+} (decreasing Ni^{2+} content), which increases the amount of mobile charge carrier. As mentioned in Figure. 8, increasing the Mn^{3+} content induces an increasing amount of unlocalized electrons which contribute to the grain conductivity.

a)

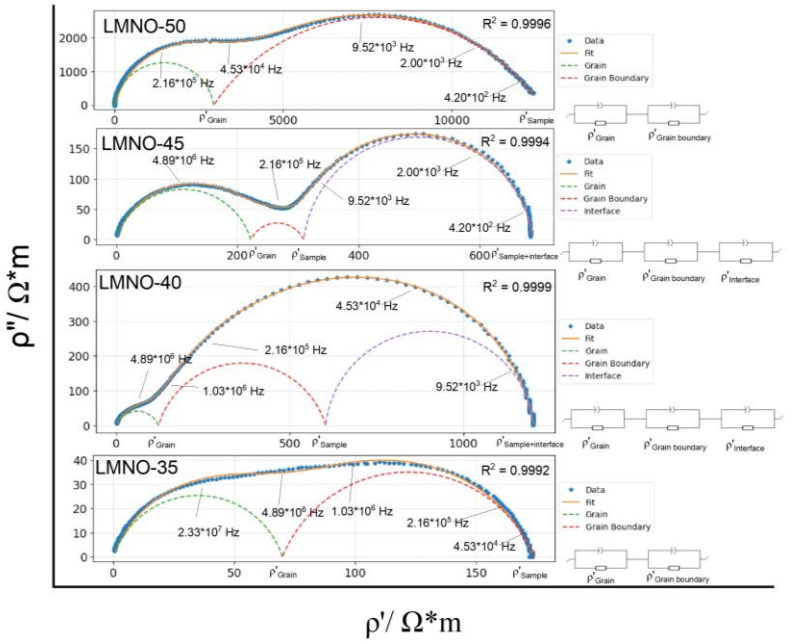

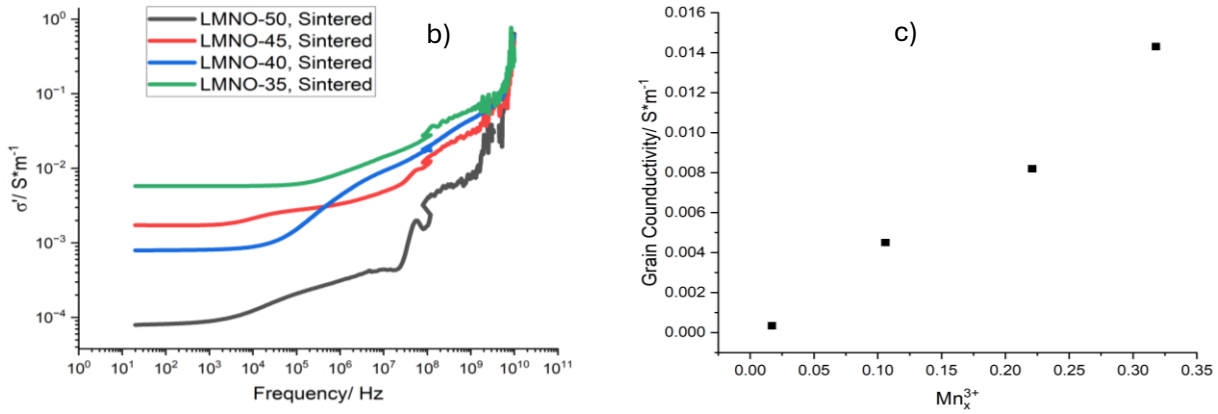

Figure.13: a) the fitted resistivity Nyquist plots using the corresponding equivalent circuit on the right. B) comparison of the real part of conductivity of the sintered materials. C) The evolution of grain's conductivity with the stoichiometry of Mn^{3+}.

The real part of the conductivity evolves with the temperature, as shown for LMNO-50, LMNO-45 and LMNO-40 in Figure. 14a. For all these samples, the conductivity decreases with decreasing the temperature. In addition, the charge transport occurring at each scale is shifted to lower frequencies when decreasing the temperature. This phenomenon is observed more clearly with the resistivity different contributions' frequency shift at selected temperatures (Figure. 14b). These observations indicate that in these materials, the conductivity is thermally activated. Therefore, from the evolution of the resistivity values determined at various temperatures, the activation energy of the charge transport process for the grain and for the sample can be determined. The conductivity of the grain is $1/\rho_{grain}$, and for the sample, it is $1/(\rho_{grain}+\rho_{grain\ boundary})$. The activation energy was determined using the Arrhenius equation shown in eq. 15 [27]. σ ($S.m^{-1}$) is the conductivity at a temperature point, σ^{o} is the conductivity pre-factor (conductivity at infinite temperature, $S.m^{-1}$), Ea is the activation energy, K is Boltzmann constant, and T is the temperature in K.

$$\sigma = \sigma^{\circ}.e^{\left(-\frac{E_a}{k.T}\right)} \ (eq.15)$$

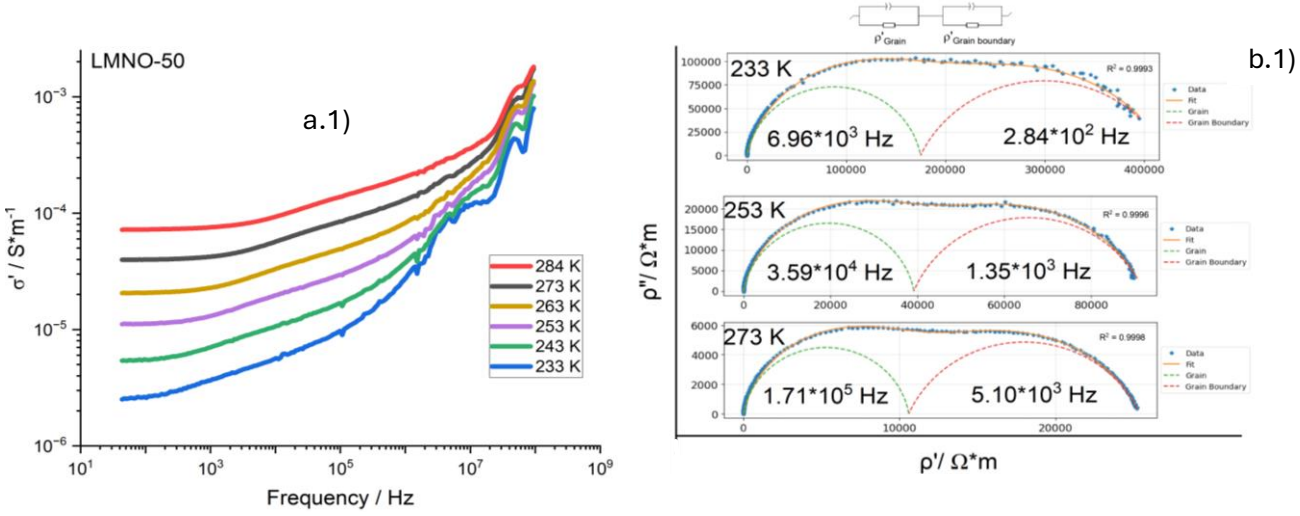

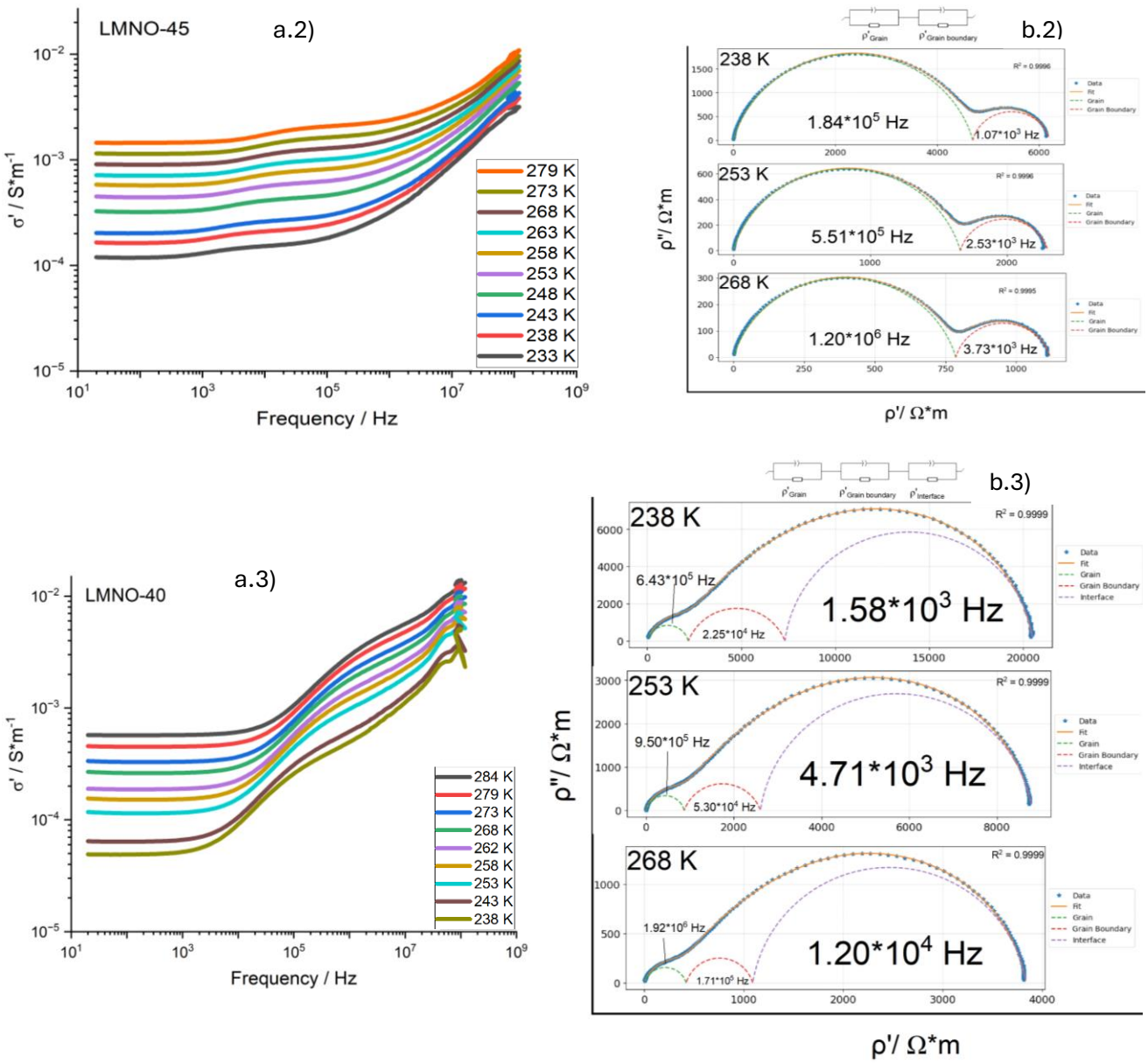

Figure. 14: (a) evolution of conductivity with temperature. (b) fitting resistivity plot at different temperature points. 1,2, and 3 are LMNO-50, LMNO-45, and LMNO-40, respectively.

Figure. 15 shows the logarithm of the conductivity versus the reverse of the temperature. Linear regression provide the activation energy Ea and ln(σ°) for each samples. For these three samples, the activation energies of the grain are similar to the activation energies of the sample. Hence, it is expected that the sintering process used to prepare the pellets lower the grain boundary resistivity since chemical bonds are present between the grains.

For both grain and sample activation energies, LMNO-50 exhibits higher values, around 0.38 eV, than LMNO-45 and LMNO-40. It is simply attributed to the presence of Mn^{3+} species, which provide more charge carriers and facilitates electron motion. Additionally, the pre-factor of the grain increases with decreasing the Ni content, which means that the number of mobile charge

carriers (electrons) increases. This is consistent with the interpretation of the conductivities at room temperature and the stoichiometry previously calculated in the galvanostatic section.

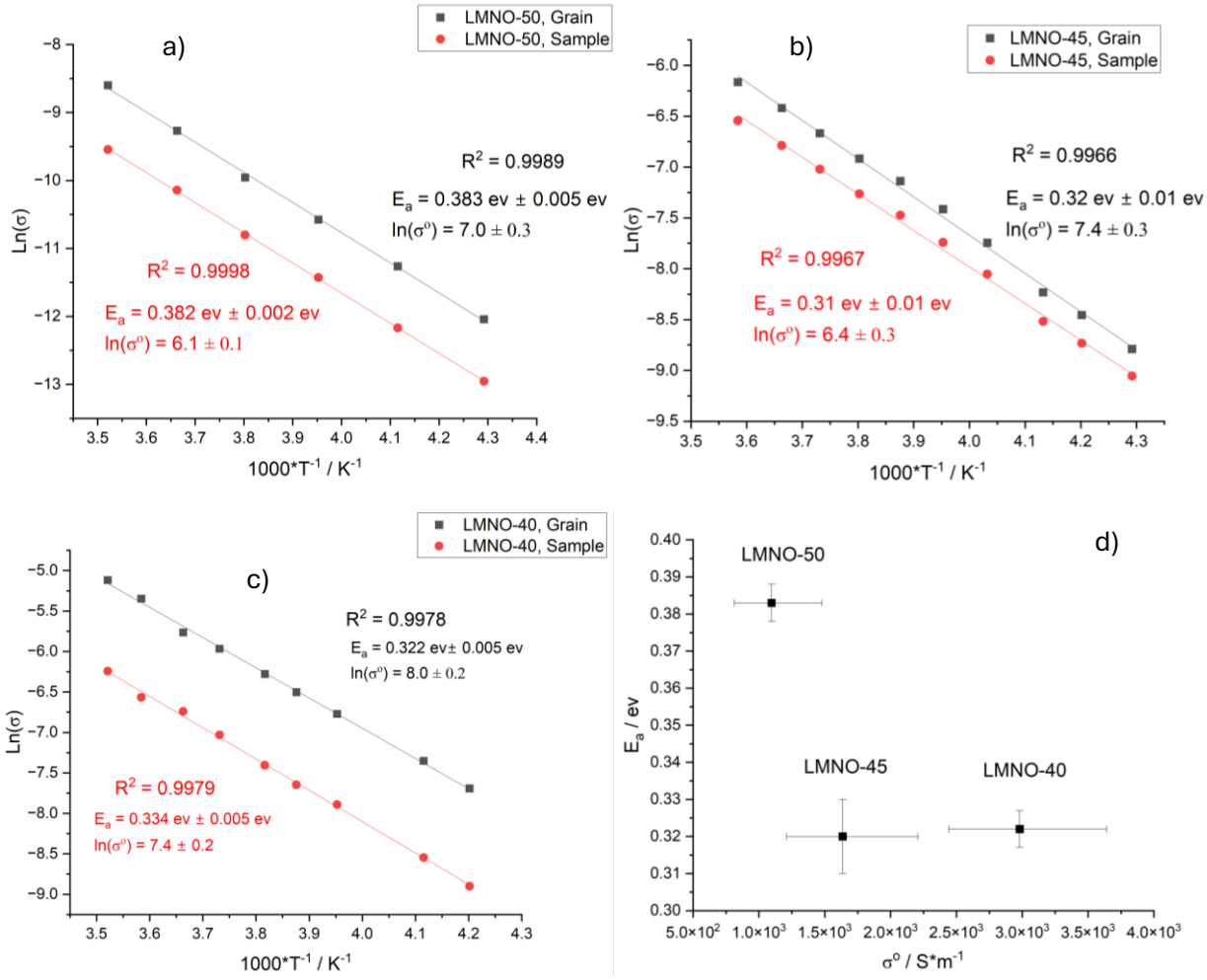

Figure 15: a, b, and c are the calculated activation energies and the natural logarithm of the conductivity pre-factor of LMNO-50, LMNO-45, and LMNO-40, respectively. The sample parameters are in red, while the grain is in black. d is the summary of the calculated parameters for the grain with their uncertainties.

Prior to the permittivity interpretation, the first resistivity contribution attributed to the sample/silver paste interface was removed by the homemade software. This step is mandatory to approach the sub-grain scale with a higher precision, since the sample/silver interface dielectric strength has significant contribution in the decomposition process, which can lead to an accumulation of error. In the case of LMNO-45, and LMNO-40, the interfacial contribution shown in Figure. 13a was successfully removed, thus, the first relaxation process observed after the straight line (static sample permittivity) is the grain polarization. For LMNO-35, the grain boundary contribution was successfully removed, thus, the first relaxation process observed after the straight line (in this case, static grain permittivity) is the polarization at the sub-grain region. For LMNO-50, the removal of the first resistivity contribution was not successful, so all the relaxation processes were decomposed. The decomposition of Nyquist permittivity spectra of LMNO-50, LMNO-45, LMNO-40, LMNO-30 is presented in Figure. 16a, b, c, and d, respectively.

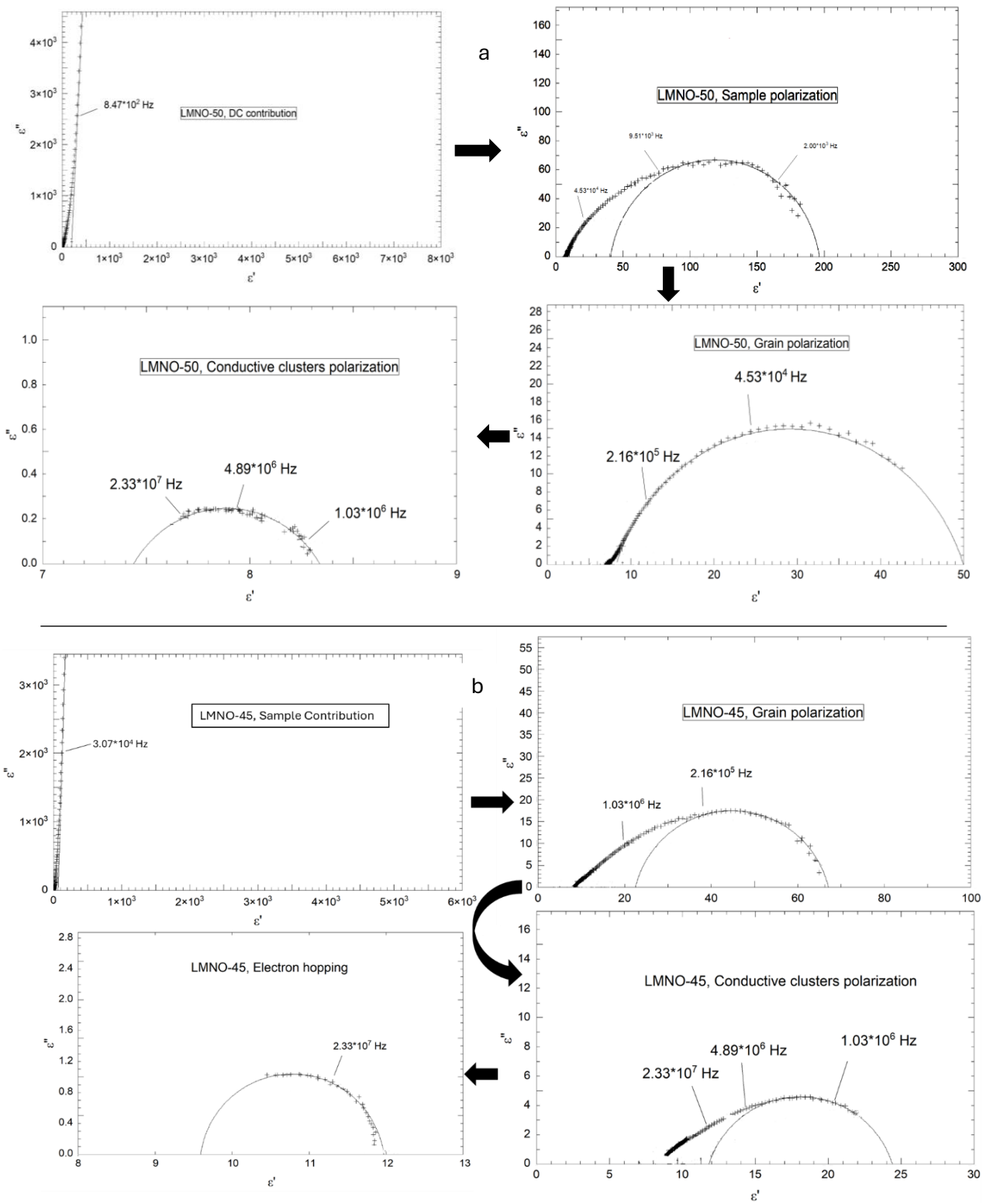
a
8.47*10² Hz
LMNO-50, DC contribution
LMNO-50, Sample polarization
9.51*10³ Hz
2.00*10³ Hz
4.53*10⁴ Hz
LMNO-50, Grain polarization
4.53*10⁴ Hz
2.16*10⁵ Hz
LMNO-50, Conductive clusters polarization
2.33*10⁷ Hz
4.89*10⁶ Hz
1.03*10⁶ Hz
b
LMNO-45, Sample Contribution
3.07*10⁴ Hz
LMNO-45, Grain polarization
2.16*10⁵ Hz
1.03*10⁶ Hz
LMNO-45, Electron hopping
2.33*10⁷ Hz
LMNO-45, Conductive clusters polarization
4.89*10⁶ Hz
1.03*10⁶ Hz
2.33*10⁷ Hz
ε'
ε"

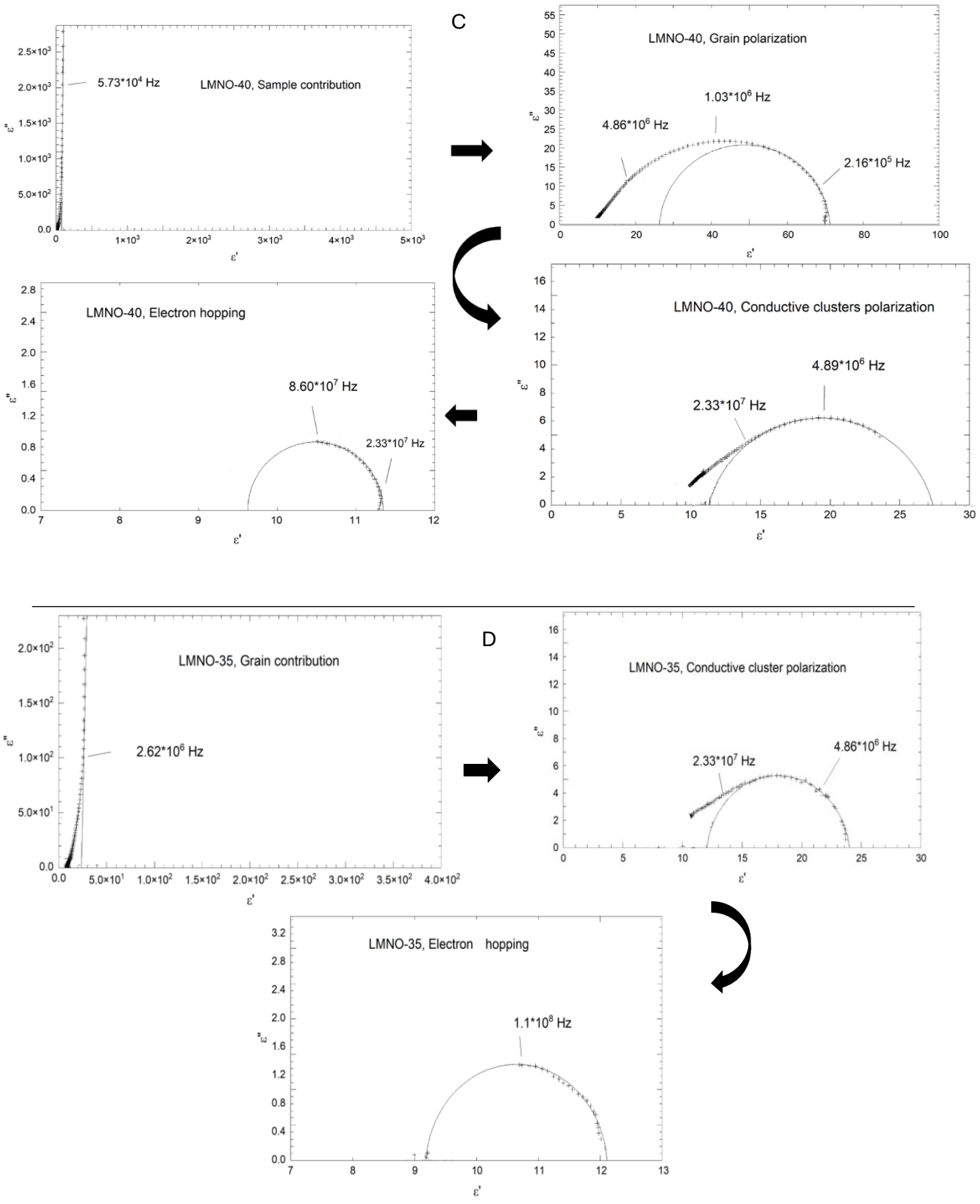

Figure.16: The Nyquist permittivity decomposition of (a)- LMNO-50, (b)- LMNO-45, (c)- LMNO-40, and (d)- LMNO-35.

The permittivity contributions of interest for all the sample are the ones in the sub-grain level (or below) as stated. All the samples show a relaxation process at this level, which is attributed to the polarization of conductive clusters. These clusters were formed due unlocalized electrons, arising from the local disorder (substitution of Ni^{2+} with Mn^{3+}, as previously demonstrated in Figure. 9b) at different sites in the grain. Furthermore, all the samples, except LMNO-50, show a contribution in the interatomic scale, which is due to electrons hopping in the cationic tetrahedral units that are inside the conductive clusters. For LMNO-50, the electron hopping contribution was not observed due to imprecise decomposition and/or the number of unlocalized electrons are so low to be detected. The evolution of the dielectric strength and the relaxation frequency of the conductive clusters is shown in Figure. 17.a. Our hypothesis of this evolution is that the clusters are percolating [28] with decreasing the Ni^{2+} content (increasing Mn^{3+} content, thus, the unlocalized electrons) as shown in Figure. 17b. Starting from LMNO-50 which has a low dielectric strength and a high relaxation frequency, which implies that the clusters have small coherence length, thus, the relaxation frequency is high. The clusters then get bigger in case of LMNO-45, which is evident from the higher dielectric strength and lower relaxation frequency relative to LMNO-50. Then percolation of the clusters occurs between Ni content of 0.45 and 0.4. Theoretically, approaching percolation threshold means the formation of clusters of an infinite coherence length, thus, infinite dielectric strength and a relaxation frequency of zero. After percolating there are two regions, the first is a percolated network of aggregated clusters, and the second region is non-percolated clusters. One should notice that the percolating network properties (i.e. dielectric strength and relaxation frequency) are not measured in the scale under investigation, as they are assumed to be too big to respond in this frequency region. For example, assuming full percolation with no clusters, the permittivity contribution under investigation will not be observed. For clusters, however, the dielectric strength gets smaller (not infinity), and the relaxation frequency gets higher as observed from the trend of LMNO-40 and LMNO-35. This is due to the increase of the percolation network at the expense of the clusters. The hypothesis could be confirmed by further expansion of the Ni content and studying the trend for more accurate estimation of the theoretical threshold point.

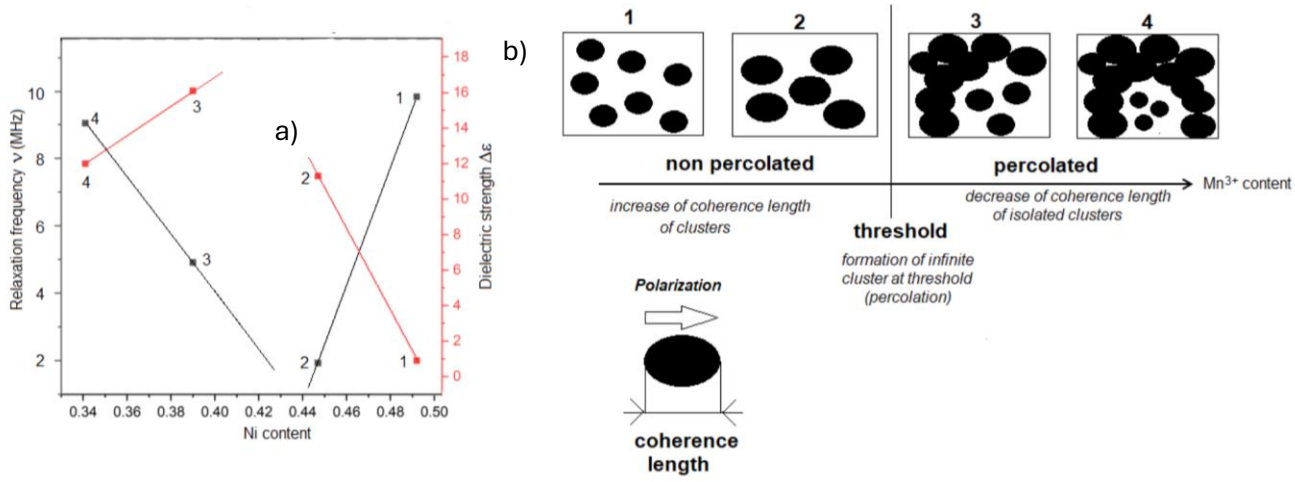

Figure. 17: 1- LMNO-50, 2-LMNO-45, 3-LMNO-40, and 4-LMNO-35. a) The evolution of dielectric strength (Δε) and relaxation frequency (ν) of the LMNO series. B) visualization of the percolation hypothesis

Conclusion and perspective

In this work, we focalized on the electronic properties of a series of LMNO sample with different nickel content and a low structural defect density. The combination of galvanostatic measurements and BDS analyses allows us to characterize the electronic conductivity of a series of LMNO with various nickel content (from 0.35 to 0.50). The galvanostatic measurements recorded at slow rate provide us an evaluation of the Mn^{3+} content in each sample. A thorough analysis of the galvanostatic curve's derivatives suggests the presence of three different types of Mn^{x+} ions for samples with nickel content ranking from 0.35 to 0.45. According to preliminary results provided by DFT calculations [24], the manganese ion which substitute a Ni^{2+} is a Mn^{3+} ion. The missing electron needed to reach the electroneutrality is distributed over the six surrounding Mn ions, leading to an average valence of +3.83. The remaining manganese ions are still Mn^{4+}, as all the manganese in $LiMn_{1.50}Ni_{0.50}O_4$. The increasing amount of Mn^{3+} ions (localized and unlocalized) with decreasing nickel content are well correlated to the increase of electronic conductivity observed from resistivity spectra. The permittivity spectra analysis suggests the presence of conductive cluster at the sub-grain scale, that is consistent with the expected electron delocalization induced by the presence of Mn^{3+}. If this work provides new insights on this promising positive electrode material family, additional work has to be done to complete this new dataset. First, additional compositions between 0.35 and 0.50 nickel content have to be synthesized and analyzed by BDS to confirm and refine the suggested percolation threshold. For instance, a precise analysis is not possible and a correlation with the structure cannot be established without additional data. In addition, the preparation of $LiMn_2O_4$ is planned to analyze the composition with the most important number of mobile charge carrier. It should provide us the maximum grain conductivity of these materials. It will help us to understand the evolution of the electronic conductivity of these systems. In addition, samples with high structural defects have to be prepared to probe the effects of the defect density of the electronic conductivity.

Acknowledgement

I am thankful to be part of the Erasmus Mundus SERP+ (Surface, Electro-, Radiation, and Photo-Chemistry) program. The experience I got from this program has set a landmark for my professional career.

My appreciation to my supervisors and co-supervisors, Dr. Olivier Dubrunfaut, Dr. Nicolas Emery, Dr. Jean-claude Badot, and Dr. Stéphane Bach for their unparalleled support and continuous guidance through my internship.

I thank the ANR (agence nationale de la recherche) for funding this project, and the institutes of Laboratoire de Génie électrique et électronique de Paris (GEEPS), and Institut de Chimie et des Matériaux Paris-Est (ICMPE, CNRS) for providing environment to conduct high-quality research.

Table of abbreviations

BDS - Broadband dielectric spectroscopy

DFT - Density functional theory

EDS - Energy-dispersive x-ray spectroscopy

e^- - electron

ID - Identity

LMNO - $LiMn_{2-x}Ni_xO_4$

LMNO-50 - $LiMn_{1.50}Ni_{0.50}O_4$

LMNO-45 - $LiMn_{1.55}Ni_{0.45}O_4$

LMNO-40 - $LiMn_{1.60}Ni_{0.40}O_4$

LMNO-35 - $LiMn_{1.65}Ni_{0.35}O_4$

LMNO-30 - $LiMn_{1.70}Ni_{0.30}O_4$

NMC - $LiNi_xMn_yCo_{1-x-y}O_2$

PTFE - polytetrafluoroethylene

SEM - Scanning electron microscopy

TGA - Thermogravimetric analysis

XRD - X-ray diffraction

References

[1] https://www.consilium.europa.eu/en/press/press-releases/2022/06/29/fit-for-55-council-reaches-general-approaches-relating-to-emissions-reductions-and-removals-and-their-social-impacts/

[2] X. Zhu, A. Huang, I. Martens, N. Vostrov, Y. Sun, M.-I. Richard, T. U. Schulli, L. Wang, High-voltage spinel cathode materials: navigating the structural evolution for lithium-ion batteries, Adv. Mater. 2024, 2403482

[3] N. Emery, A. Bhatia, Y. Ghaleb, A. Mitrushchenkov, C. Léonard, JP. Pereira-Ramos, R. Baddour-Hadjean, R.I. Smith, Chem. Mater. 34 (2022) 3152-3167

[4] W. Li, B. Song, A. Manthiram, High-voltage positive electrode materials for lithium-ion batteries. Chem. Soc. Rev. 2017, 46, 3006−3059.

[5] J. Liu, A. Huq, Z. Moorhead-Rosenberg, A. Manthiram, K. Page, Nanoscale Ni/Mn ordering in the high voltage spinel cathode LiNi0.5Mn1.5O4. Chem. Mater. 28 (2016) 6817−6821.

[6] M. Casas-Cabanas, C. Kim, J. Rodriguez-Carvajal, J. Cabana, Atomic defects during ordering transitions in LiNi0.5Mn1.5O4 and their relationship with electrochemical properties. J. Mater. Chem. A 4 (2016),8255−8262.

[7] Broadband dielectric spectroscopy.I.Kremer,F.(Friedrich),1949-II.Schönhals, A.(Andreas) QC454.B74 B76 2002, page 10.

[8] Broadband dielectric spectroscopy.I.Kremer,F.(Friedrich),1949-II.Schönhals, A.(Andreas) QC454.B74 B76 2002, page 23.

[9] J.C. Badot, E. Ligneel, O. Dubrunfaut, J. Gaubicher, D. Guyomard, B. Lestriez, B. Influence of adsorbed polar molecules on the electronic transport in a composite material Li1.1V3O8–PMMA for lithium batteries. *Physical Chemistry Chemical Physics*, *14* (2012) 9500.

[10] Broadband dielectric spectroscopy.I.Kremer,F.(Friedrich),1949-II.Schönhals, A.(Andreas) QC454.B74 B76 2002, page 38.

[11] A.A. Lukichev, Relaxation function for the non-debye relaxation spectra description. *Chemical Physics*, *428* (2014) 29–33.

[12] J.C. Badot, B. Lestriez, O. Dubrunfaut, Interest in broadband dielectric spectroscopy to study the electronic transport in materials for lithium batteries. *Materials Science and Engineering: B*, *213* (2016) 190–198.

[13] L. Batyuk, N. Kizilova. Modeling of Dielectric Permittivity of the Erythrocytes Membrane as a Three-Layer Model. 2018.

[14] A.C. Larson, R.B. Von Dreele, General Structure Analysis System (GSAS); Los Alamos National Laboratory: Los Alamos, NM, 2004; Technical Report No. LAUR86-748.

[15] N.-E. Belhadj-Tahar, A. Fourrier-Lamer, H. de Chanterac, Broad-Band Simultaneous Measurement of Complex Permittivity and Permeability Using a Coaxial Discontinuity. IEEE Transactions On Microwave Theory And Techniques vol. 38 (1990).

[16] L. Beluze, J.C. Badot, R. Weil, V. Lucas, Broadband dielectric and resistivity spectroscopy of Wo3·H2O in the range of 103−1010 hz: particle size effect. *The Journal of Physical Chemistry B*, *110* (2006) 7304–7308.

[17] N.E. Belhadj-Tahar, O. Dubrunfaut, A. Fourrier-Lamer, Equivalent Circuit for Coaxial Discontinuities Filled With Dielectric Materials - Frequency Extension of the Marcuvitz's Circuit. *Journal of Electromagnetic Waves and Applications*, *15* (2001) 727–743.

[18] M.D. Murbach, B. Gerwe, N. Dawson-Elli, L.Tsui, impedance.py: A Python package for electrochemical impedance analysis. Journal of Open Source Software, 5 (2020) 2349.

[19] Z. Wang, J. Du, W. Duan, Y. Niu, Z. Wu, LiMn2-xNixO4 Spinel Oxides as High-Temperature Lithium Battery Cathode Materials for Borehole Applications, International Journal of Electrochemical Science, 8, (2013) 6231-6242.

[20] J. Cen, B. Zhu, S.R. Kavanagh, A.G. Squires, D.O. Scanlon, Cation disorder dominates the defect chemistry of high-voltage limn1.5ni0.5O4 (LMNO) spinel cathodes. *Journal of Materials Chemistry A*, *11* (2023) 13353–13370.

[21] R. D. Shannon, *Revised Effective Ionic Radii and Systematic Studies of Interatomic Distances in Halides and Chalcogenides,* Acta Cryst. A (1976) 32, 751-767

[22] J. Cabana, H. Zheng, A.K. Shukla, C. Kim, V.S. Battaglia, M. Kunduraci, Comparison of the performance of LiNi1/2Mn3/2O4 with different microstructures. J. Electrochem. Soc. 158 (2011) A997−A1004.

[23] P. Stüble, V. Mereacre, H. Geßwein, J. R. Binder, On the Composition of $LiNi_{0.5}Mn_{1.5}O_4$ Cathode Active Materials. *Adv. Energy Mater.* 13 (2023) 2203778.

[24] A. Mitrushchenkov, E. Mangaud, C. Léonard, N. Emery, MSME, unpublished results.

[25] K. Ariyoshi, Y. Iwakoshi, N. Nakayama, T. Ohzuku, Topotactic Two-Phase Reactions of LiNi1/2Mn3/2O4 (P4332) in Nonaqueous Lithium Cells, J. Electrochem. Soc., 151 (2004) A296-A303

[26] N. Bonanos, P. Pissis, J.R. Macdonald, (2012) Impedance Spectroscopy of Dielectrics and Electronic Conductors. In Characterization of Materials, E.N. Kaufmann (Ed.).

[27] T.T. Lin, S.L. Young, C.Y. Kung, H.Z. Chen, M.C. Kao, M. C. Chang, C.R. Ou, Variable-range hopping and thermal activation conduction of Y-doped zno nanocrystalline films. *IEEE Transactions on Nanotechnology*, *13* (2014) 425–430.

[28] S. Kirkpatrick. Percolation and Conduction. Rev. Mod. Phys. (1973) 45(4), 574-588.